Enhanced second-harmonic generation from magnetic resonance in AlGaAs nanoantennas

Costantino de Angelis, Andrea Locatelli, Luca Carletti, Davide Rocco, Oleksandr Stepanenko, Giuseppe Leo, Ivan Favero, Aristide Lemaitre, Giuseppe Marino, Nicolas Olivier, et al.

Enhanced second-harmonic generation from magnetic resonance in AlGaAs nanoantennas

Costantino De Angelis*[a], Andrea Locatelli[a], Luca Carletti[a], Davide Rocco[a], Oleksandr Stepanenko[b], Giuseppe Leo[b], Ivan Favero[b], Aristide Lemaitre[c], Giuseppe Marino[d], Nicolas Olivier[d], Anatoly V. Zayats[d]

[a]Dept. of Information Engineering, University of Brescia, Via Branze 38, 25123, Brescia, Italy; [b]Laboratoire Matériaux et Phénomènes Quantiques, Université Paris Diderot—CNRS, Sorbonne Paris Cité, 10 rue Alice Domon et Léonie Duquet, F-75013 Paris, France; [c]Laboratoire de Photonique et Nanostructures, CNRS-UPR20, Route de Nozay, 91460 Marcoussis, France. [d]Department of Physics, King's College London, Strand, London, WC2R 2LS, UK

*costantino.deangelis@unibs.it

ABSTRACT

We designed cylindrical AlGaAs-on-aluminium-oxide all-dielectric nanoantennas with magnetic dipole resonance at near-infrared wavelengths. Our choice of material system offers a few crucial advantages with respect to the silicon-on-insulator platform for operation around 1.55μm wavelength: absence of two-photon absorption, high $\chi^{(2)}$ nonlinearity, and the perspective of a monolithic integration with a laser. We analyzed volume second-harmonic generation associated to a magnetic dipole resonance in these nanoantennas, and we predict a conversion efficiency exceeding 10^{-3} with 1GW/cm^2 of pump intensity.

Keywords: All-dielectric nanoantennas, nonlinear nanophotonics, second harmonic generation, Mie scattering, AlGaAs.

1. INTRODUCTION

Optical nanoantennas is a rapidly expanding field of research owing to the huge number of potential applications such as biosensing, photovoltaics, telecommunications and nanomedicine[1,2]. The key optical property of these structures is the capability to mold the flow of light at subwavelength length scales. Since the last decade, the advance in the fabrication techniques made accessible a precise and controllable fabrication of metallic nanostructures, allowing the flourishing of the field of nanoplasmonics. The optical properties of such structures are due to the possibility of the excitation of localized surface plasmon resonances (LSPR), i.e. resonant collective oscillations of the conduction electrons near the surface of the metal, in the visible and near-infrared (near-IR) wavelength range[1]. Furthermore, the characteristics of the LSPRs can be predicted using design guidelines which have been developed starting from well-established techniques already in use at microwave frequencies[3,4]. However, metals suffer from large resistive heating losses that severely limit the performance of devices[5,6]. In this context, semiconductor nanoparticles are emerging as a promising alternative to metallic ones for a wide range of nanophotonic applications based on localized resonant modes in the entire visible and near-IR spectral ranges, see e.g. Refs. [5–12]. All-dielectric optical nanoantennas consist of high-permittivity low-loss dielectric particles of submicrometer size in a low-permittivity environment. The absence of plasmonic excitations strongly reduces the ohmic losses that affect metals. Furthermore, as it was recently observed[9–11], dielectric nanoantennas can exhibit both strong electric and magnetic optical resonances in the wavelength range from the visible to the near-IR.

All-dielectric nanoantennas can be realized by using different particle geometries, but mainly spherical and cylindrical antennas have been dealt with to date. Spherical shaped nanoantennas have the advantage of easy and fast prediction of the resonant peaks in the spectrum by using the well-known Mie theory[13]. On the other hand, nanodisks have recently proven to be versatile in tailoring of electric and magnetic response, stemming from two degrees of freedom: radius and height[14,15]. In addition, as opposed to nanospheres, the fabrication of nanodisks is easily accessed by modern electron beam lithography, which enables a precise control of the nanodisk size and lattice geometries. Dielectric nanostructures on a low-index substrate have been recently demonstrated in the framework of semiconductor planar technology, encompassing the cases of silicon-on-insulator (SOI)[16], as well as GaAs on silica[10]. In the present work, we developed a

fabrication technique to obtain AlGaAs-on-aluminum-oxide monolithic nanoantennas. This new material system will allow to fully exploit all the advantages of this mature III-V platform including the direct integration of sources, e.g. diode lasers, nanostructures and detectors on a GaAs chip.

All-dielectric nanoantennas offer unique opportunities for the study of nonlinear effects due to very low losses in combination with multipolar characteristics of both electric and magnetic resonant optical modes[16,17]. The nonlinear optical effects of magnetic origin can have fundamentally different properties compared with those of electric origin. When nonlinearities of both electric and magnetic type are present, the nonlinear response can be substantially modified and nonlinear mode mixing and magnetoelectric coupling effect might be observed[18,19]. To the best of our knowledge, the only experimental investigations of the nonlinear optical response generated from a magnetic resonant optical mode in an all-dielectric antenna have been conducted on Si nanodisks[14,16]. However, in that case, operation in the third window of optical fiber communication is limited by two-photon absorption (TPA) and volume $\chi^{(2)}$ interactions are absent because of centro-symmetry of Si. In this perspective III-V materials such as GaAs or AlGaAs offer a strong potential to efficiently observe second order nonlinear effects such as Second-Harmonic Generation (SHG)[17]. Furthermore, by engineering the AlGaAs alloy composition, TPA at wavelengths close to 1.55μm can be avoided, thus further enhancing the efficiency of the observable nonlinear phenomena.

In this work, we study the linear and nonlinear scattering of AlGaAs-on-aluminum-oxide monolithic nanodisks. In Section 2, we illustrate the design of nanodisks exhibiting the magnetic dipole (MD) resonance in the near-IR wavelength range. In Section 3, we report, for the first time, an analysis of the optical nonlinear response generated from volume $\chi^{(2)}$ nonlinearity in all-dielectric nanodisks. Our results show that AlGaAs nanoantennas have a strong potential to enhance the SHG from all-dielectric nanostructures. In Section 4 we illustrate the fabrication of AlGaAs-on-aluminum-oxide monolithic nanoantennas with the most promising designs.

2. LINEAR SCATTERING OF AlGaAs NANOANTENNAS

We investigated the scattering characteristics of $Al_{0.18}Ga_{0.82}As$ cylinders at near-IR wavelengths by using frequency domain simulations with finite element method in COMSOL. As shown in the inset of Fig. 1(a), the incident light was a plane wave with a wave vector, **k**, parallel to the cylinder axis and the electric field, **E**, polarized along the x-axis.

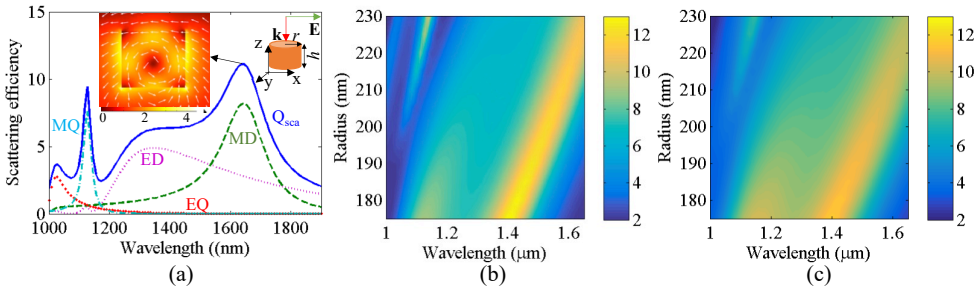

Fig. 1. (a) Scattering efficiency Q_{sca}, decomposed in magnetic dipole (MD), electric dipole (ED), magnetic quadrupole (MQ), and electric quadrupole (EQ) contributions, as a function of wavelength calculated for r=225 nm and h=400 nm. A schematic of the AlGaAs cylinder with the incident field and the cross section of normalized |**E**| in the x-z plane through the axis of the cylinder are shown in the inset. The arrows represent **E** in the same x-z plane. (b) and (c) scattering efficiency as a function of wavelength and cylinder radius for a constant height h=400 nm for cylinders suspended in air and on a substrate with n=1.6 respectively.

For the dispersion of the refractive index of $Al_{0.18}Ga_{0.82}As$ we used the analytical model proposed in Ref. [20] which was derived from comparison with measurements. The scattering efficiency (defined as $Q_{sca}=C_{sca}/\pi r^2$ where C_{sca} is the scattering cross-section and r is the cylinder radius) calculated for a cylinder with radius r=225 nm and height h=400 nm is shown in Fig. 1(a). We can observe that several resonant peaks appear at wavelengths shorter than about λ=1700 nm while, for longer wavelengths, the scattering efficiency monotonically decreases. For gaining further insight into the scattering mechanisms, the contribution from the different multipole orders to the total scattering efficiency is also shown in Fig. 1(a). This was calculated by evaluating the overlap integral between the scattered electric field and the spherical harmonics on a spherical surface enclosing the antenna[21]. As it can be noted in Fig. 1(a), the sharper and strongest resonance observed at λ=1640 nm is mainly due to a MD resonance. The electric field distribution at this resonance is shown in the inset of Fig. 1(a). Because the incident electric field was x-polarized, the main components of the electric field inside the cylinder are along the x and z directions. The broader resonance at λ=1300 nm is of electric

dipole type while higher-order multipoles contribute to the resonances observed at shorter wavelengths (see Fig. 1(a)). When the geometric parameters of the antenna are changed, the resonances observed in Fig. 1(a) shift in wavelength. The scattering efficiency of cylinders with radius varying from 175 nm up to 230 nm and a constant height of 400 nm is shown in Fig. 1(b). It can be seen that the resonant peaks red-shift as the radius of the cylinder is increased. For example, the MD resonance peak wavelength shifts from λ=1410 nm when r=175 nm up to λ=1655 nm when r=230 nm. This effect is expected since as the dimension of the cylinder increases, at resonance, a larger fraction of the field is inside the cylinder of high refractive index medium[14]. The scattering efficiency for cylinders of the same sizes as the ones in Fig. 1(b), but placed on a substrate with a refractive index of 1.6, is shown in Fig. 1(c). This configuration reflects the case of the antennas fabricated onto an aluminum oxide substrate. We can see that the effect of the substrate on the scattering efficiency is small (e.g. for r=220 nm the MD resonance wavelength is about 1620 nm in the case without the substrate and 1630 nm with the substrate). The presence of the substrate does not radically alter the scattering efficiency of the nanoantennas due to the large difference between the refractive index of the AlGaAs nanodisk and the aluminum oxide substrate. This shows that the AlGaAs-on-aluminum-oxide material system is a strong candidate for the realization of monolithic efficient nanoantennas.

3. SECOND HARMONIC GENERATION

Second harmonic generation in plasmonic nanostructures has been deeply investigated in recent years, often enhanced by matching LSPR either with the excitation or the emission wavelength[2,22,23]. Furthermore, SHG from metal-dielectric-metal metasurfaces has been studied[24]. In all these cases the main contribution to the second harmonic (SH) signal came from the surface nonlinearity of the metal while the volume contribution was negligible. In this work, since AlGaAs is a non-centrosymmetric material, we have a strong volume contribution which could enhance the SH signal[17]. We first note that, among the different resonant modes that have been observed in the nanodisks, for example in Fig. 1(a), the MD resonance shows the strongest scattering efficiency. This can potentially enhance the nonlinear optical response achievable from these nanoantennas.

In order to illustrate the potential of AlGaAs cylinders for nonlinear nanophotonics, let us investigate the SHG phenomenon by using the nonlinear polarization induced by $\chi^{(2)}$ as a nonlinear current source in frequency domain simulations. Here we considered $Al_{0.18}Ga_{0.82}As$ oriented along the $[\bar{1}00]$ crystalline axis for which the only non-zero elements of the second order nonlinear susceptibility are $\chi^{(2)}_{ijk} = 100$ pm/V for $i \neq j \neq k$ [25]. Moreover, we define the SHG efficiency as[17]

$$\eta_{SHG} = \frac{\int_A \vec{S}_{SH} \cdot \hat{n}\, da}{I_0 \times \pi r^2} \tag{1}$$

where $\vec{S}_{SH}$ is the Poynting vector of the SH field, $\hat{n}$ is the unit vector normal to a surface A enclosing the antenna, and I_0 is the incident field intensity (I_0=1 GW/cm^2 in the simulations). The calculated SHG efficiency as a function of the pump wavelength for a cylinder with r=225 nm and h=400 nm suspended in air is shown in Fig. 2(a). As it can be seen, the maximum SHG efficiency is obtained for a pump wavelength of λ=1675 nm, which is close to the MD resonance wavelength (i.e. λ=1640 nm, see Fig. 1(a)).

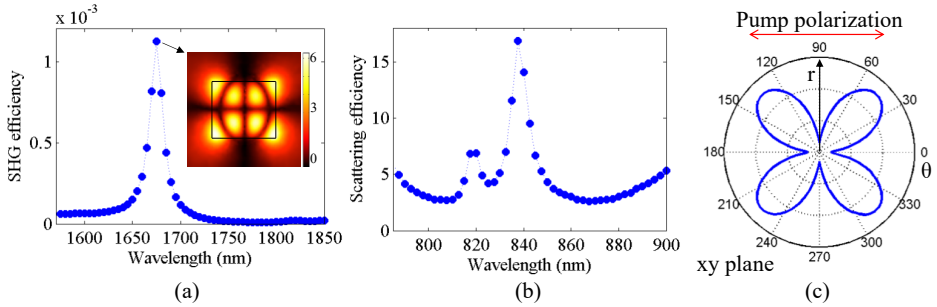

Fig. 2. (a) SHG efficiency as a function of pump wavelength for a cylinder with r=225 nm, h=400nm suspended in air and pump intensity I_0=1GW/cm^2. The normalized $|\mathbf{E}^{SH}|$ on a cross section in the x-z plane at the center of the cylinder is

shown in the inset. (b) Scattering efficiency at wavelengths between 785 nm and 900 nm. (c) Far-field radiation pattern of the SH electric field in the x-y plane.

One would normally expect to observe the strongest enhancement of the SHG when pumping at the MD resonance. Therefore, in order to understand why the maximum of η_{SHG} was not obtained for a pumping wavelength of λ=1640 nm, we calculated the linear scattering efficiency for wavelengths between 785 nm and 900 nm (shown in Fig. 2(b)). We can observe that there is a resonance at λ=837.5 nm that can explain the SHG efficiency enhancement when pumping at λ=1675 nm. Another resonance is found at λ=820 nm, that is exactly at half the MD resonance peak. However, the SHG efficiency using a pump wavelength of 1640 nm (thus matching the MD resonance) is smaller than the one obtained with a pump wavelength of 1675 nm. In order to clarify this point, we evaluated the overlap integral defined as[17]

$$\zeta = \frac{\left|\int E_x^{FF} E_z^{FF} \left(E_y^{SH}\right)^* dV\right|}{\sqrt{\int\left|E_x^{FF} E_z^{FF}\right|^2 dV}\sqrt{\int\left|E_y^{SH}\right|^2 dV}} \tag{2}$$

where E_i^{FF} and E_i^{SH} are the components of the electric field along the *i*-axis for the pump and the emission, or SH, modes, respectively. In the overlap integral we considered only this combination of fields because of two reasons. First, the main components of the electric field at the MD resonance are those in the *x* and *z* axis. Second, the only non-zero terms of the second order nonlinear susceptibility are those with $i \neq j \neq k$. The overlap integral between the mode at λ=820 nm and the mode at the pump wavelength of 1640 nm is only about 14%, whereas ζ is about 54% between the modes at λ=837.5 nm and λ=1675 nm (i.e. where the maximum of η_{SHG} is observed, see Fig. 2(a)). Therefore, since the MD resonance is spectrally broader than the resonances in the wavelength range corresponding to the SH signal, the SHG efficiency depends strongly on the overlap between the modes at the emission and pump wavelength. The magnitude of the electric field of the SH signal generated with a pump at λ=1675 nm is shown in the inset of Fig. 2(a). The far-field radiation pattern is shown in Fig. 2(c) and we can recognize a quadrupolar emission pattern.

Figure 3(a) provides the SHG efficiency as a function of pump wavelength and cylinder radius. The peak wavelength of SHG efficiency redshifts as *r* is increased, following the resonant mode at the emission wavelength (red dotted line) that was found to have a good overlap with the MD resonance (white dotted line). The maximum SHG efficiency as a function of the cylinder radius is extracted along the red-dotted line of Fig. 3(a) and shown in Fig. 3(b) (blue dots). We can observe that the wavelength at which the SH signal is generated varies from 788 nm to 848 nm as *r* is varied between 202 nm and 235 nm. Furthermore, the SHG efficiency varies only of about 10% in the same range of radii, which might be due to the fact that the MD resonance is spectrally broader than the SH resonance (compare Fig. 1(a) and Fig. 2(b)).

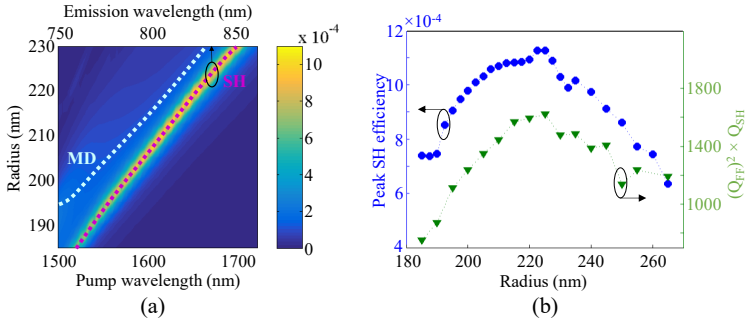

Fig. 3. (a) SHG efficiency as a function of pump wavelength and nanodisk radius. The magnetic dipole resonance (MD) and the resonant mode at the emission wavelength (SH) are outlined with a dotted white and magenta line respectively. (b) Maximum SHG efficiency (circles) and $(Q_{FF})^2 \times Q_{SH}$ (triangles) as a function of nanodisk radius. The nanodisks have constant height of 400 nm and are suspended in air. The pump intensity is 1GW/cm^2.

As it can be seen in Fig. 3(b), η_{SHG} initially increases as the cylinder radius is increased and, after a maximum when *r*=225 nm, it decreases. This behavior can be intuitively explained by evaluating $\upsilon = (Q_{FF})^2 \times Q_{SH} \times \zeta$, where Q_{FF} and Q_{SH} are the scattering efficiency of the pump and second-harmonic modes respectively. The conversion efficiency is expected to increase as Q_{FF}^2 because the intensity of the SH signal scales as the squared power of the electric field intensity of the pump beam. Indeed, if we evaluate υ for the cylinder with *r*=225nm, we obtain a maximum at λ=1675 nm, in good agreement with the results shown in Fig. 2(a). When the radius is varied, ζ remains almost constant while the spectral distance between the wavelength of the pump for which η_{SHG} is maximum and the MD resonance increases (see dotted

lines in Fig. 3(a)). Therefore, Q_{FF} diminishes which in turn lowers υ, in good agreement with the results shown in Fig. 3(b). Furthermore, we analyzed the SHG efficiency for cylinders with different heights (between 300nm and 600nm). We observe that the overlap integral ζ between the pump and the SH mode remains almost unchanged as the height is varied. When the height of the cylinder is decreased, the spectral distance between the SH mode and the MD mode increases. Thus, the maximum of η_{SHG} decreases because the product $(Q_{FF})^2 \times Q_{SH}$ decreases. When the cylinder height is increased, the spectral distance between the pump and the MD mode progressively decreases and the pump wavelength can eventually coincide with the MD resonance for h=600 nm and r=300 nm. Despite this fact, we observed that the maximum SHG efficiency is smaller than the one obtained for the cylinder with h=400 nm. In fact, when the height of the cylinder is increased, Q_{SH} decreases and thus υ decreases as well. From these observations, it is straightforward to understand that in order to maximize η_{SHG}, the nanoparticle geometry should be engineered for, from one side, guaranteeing a fair tradeoff between the need of a high Q_{FF} and a high Q_{SH} to maximize the product $(Q_{FF})^2 \times Q_{SH}$ and, from the other side, optimizing the spatial overlap ζ of the nanoparticle mode at the SH wavelength with the pump mode.

4. FABRICATION

Recently, a hybrid solution for tight vertical confinement of light at 1.55 μm in TPA-free material was proposed by Yvind et al., relying on a thin AlGaAs film on a SiO_2 insulator layer, through wafer bonding and substrate removal[26]. The present work, conversely, stems from our choice of AlGaAs-on-aluminum-oxide monolithic nanoantennas, as a mean to fully exploit all the advantages of this mature III-V platform. This approach is an extension of the use of selectively oxidized thin AlAs layers within AlGaAs optical heterostructures, both as a phase-matching tool in form-birefringent $\chi^{(2)}$ waveguides[27] and in the fabrication of VCSELs[28]. While the selective lateral oxidation of such AlAs layer (which gives rise to "AlOx" non-stoichiometric layers with typical thickness of a few tens of nanometers) is a well-known process, its application to the oxidation of thicker optical substrates requires special care, in order to avoid that the stress induced by AlAs contraction.

Our samples were grown by molecular-beam-epitaxy on $[\bar{1}00]$ non-intentionally doped GaAs wafer, with a 400 nm layer of $Al_{0.18}Ga_{0.82}As$ on top of an aluminum-rich substrate, to be oxidized at a later stage. In order to improve the eventual adhesion between AlOx and the adjacent crystalline layers, such substrate consists of AlAs layer of about 1μm of thickness.

In order to obtain an array of nanodisks as shown in Fig. 4(a), we patterned circles with radii between 180 nm and 220 nm, and equally spaced by 3 μm, with a scanning electron microscope (SEM) Zeiss lithography system.

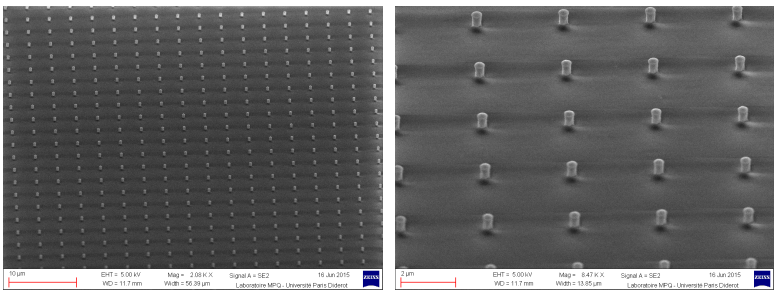

(a) (b)

Fig. 4. SEM images of $Al_{0.18}Ga_{0.82}As$ nanodisks after oxidation of bottom AlAs layer.

Then our samples were dry etched with non-selective ICP-RIE (Sentech SI500) with $SiCl_4$:Ar chemical treatment. The etching depth of 400 nm, controlled by laser interferometer, defined the nano-cylinders and revealed the AlAs layer as it can be seen in Fig. 4(b). Then the etched sample was placed in an oxidation oven equipped with an in situ optical control (Fig. 5).

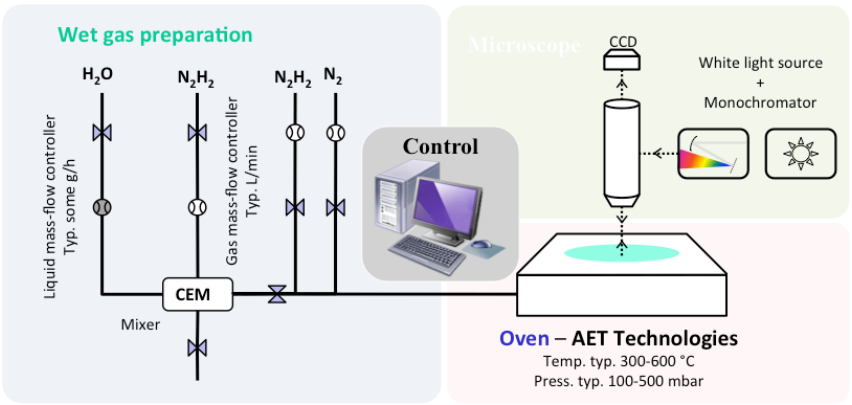

Fig. 5. Schematics of the system for the oxidation of AlGaAs heterostructures.

5. CONCLUSION

In this work, we reported the design and fabrication of AlGaAs on aluminum-oxide nanoantennas for applications in nonlinear nanophotonics. We showed that by varying height and radius of the nanodisk the AlGaAs nanoantennas could sustain a strong MD resonance in the near-IR wavelength range. Simulation results also showed a small difference in the optical response of the nanoantennas when a substrate with a refractive index similar to aluminum-oxide is considered. These nanoantennas have been used for studying the SHG phenomenon when the pump wavelength is chosen close to the MD mode. This is the first investigation of volume second-order nonlinear optical interactions generated from a MD resonance in all-dielectric nanoantennas. We found that in order to achieve a strong enhancement of the conversion efficiency it is necessary to have a good mode overlap and a strong scattering efficiency of both the pump and the SH mode. Using frequency domain simulations, we predicted a SHG efficiency larger than 10^{-3} from a single nanodisk with r=225nm and h=400nm and using a pump intensity of I_0=1GW/cm^2 at a wavelength of 1675 nm. Furthermore, we developed a technique to fabricate these antennas using the AlGaAs-on-aluminum-oxide material system. Our material choice can be advantageous under several perspectives. As far as the nonlinear optical properties are concerned, AlGaAs is a highly nonlinear material with both $\chi^{(2)}$ and $\chi^{(3)}$ nonlinearities and TPA can be avoided at near-IR wavelengths by engineering the alloy composition. Furthermore, the maturity of this III-V material platform can be exploited to realize monolithically integrated devices with, for instance, integrated laser source on chip.

REFERENCES

[1] Schuller, J. A., Barnard, E. S., Cai, W., Jun, Y. C., White, J. S., Brongersma, M. L., "Plasmonics for extreme light concentration and manipulation," Nat. Materials **9**(3), 193–204, Nature Publishing Group (2010).

[2] Kauranen, M., Zayats, A. V., "Nonlinear Plasmonics," Nat. Photonics **6**, 737–748, Nature Publishing Group (2012).

[3] Alù, A., Engheta, N., "Input impedance, nanocircuit loading, and radiation tuning of optical nanoantennas," Phys. Rev. Lett. **101**(4), 043901 (2008).

[4] Locatelli, A., De Angelis, C., Modotto, D., Boscolo, S., Sacchetto, F., Midrio, M., Capobianco, A.-D., Pigozzo, F. M., Someda, C. G., "Modeling of enhanced field confinement and scattering by optical wire antennas," Opt. Express **17**(19), 16792–16800 (2009).

[5] Ginn, J. C., Brener, I., Peters, D. W., Wendt, J. R., Stevens, J. O., Hines, P. F., Basilio, L. I., Warne, L. K., Ihlefeld, J. F., et al., "Realizing optical magnetism from dielectric metamaterials," Phys. Rev. Lett. **108**(9), 097402 (2012).

[6] Albella, P., Alcaraz de la Osa, R., Moreno, F., Maier, S. A., "Electric and Magnetic Field Enhancement with Ultralow Heat Radiation Dielectric Nanoantennas: Considerations for Surface-Enhanced Spectroscopies," ACS Photonics **1**(6), 524–529 (2014).

[7] Decker, M., Staude, I., Falkner, M., Dominguez, J., Neshev, D. N., Brener, I., Pertsch, T., Kivshar, Y. S., "High-Efficiency Dielectric Huygens' Surfaces," Adv. Opt. Mater. **3**, 813–820 (2015).

[8] Krasnok, A. E., Miroshnichenko, A. E., Belov, P. A., Kivshar, Y. S., "All-dielectric optical nanoantennas.," Opt. Express **20**(18), 20599–20604 (2012).
[9] Evlyukhin, A. B., Novikov, S. M., Zywietz, U., Eriksen, R. L., Reinhardt, C., Bozhevolnyi, S. I., Chichkov, B. N., "Demonstration of magnetic dipole resonances of dielectric nanospheres in the visible region," Nano Lett. **12**(7), 3749–3755 (2012).
[10] Person, S., Jain, M., Lapin, Z., Sáenz, J. J., Wicks, G., Novotny, L., "Demonstration of zero optical backscattering from single nanoparticles," Nano Lett. **13**(4), 1806–1809 (2013).
[11] Gómez-Medina, R., García-Cámara, B., Suárez-Lacalle, I., González, F., Moreno, F., Nieto-Vesperinas, M., Sáenz, J. J., "Electric and magnetic dipolar response of Germanium spheres: Interference effects, scattering anisotropy and optical forces," J. Nanophotonics **5**, 053512 (2011).
[12] García-Etxarri, A., Gómez-Medina, R., Froufe-Pérez, L. S., López, C., Chantada, L., Scheffold, F., Aizpurua, J., Nieto-Vesperinas, M., Sáenz, J. J., "Strong magnetic response of submicron silicon particles in the infrared.," Opt. Express **19**(6), 4815–4826 (2011).
[13] Bohren, C. F., Huffman, D. R., Absorption and Scattering of Light by Small Particles, Wiley-VCH Verlag GmbH (2007).
[14] Groep, J. Van De., Polman, A., "Designing dielectric resonators on substrates : Combining magnetic and electric resonances," Opt. Express **21**(22), 1253–1257 (2013).
[15] Staude, I., Miroshnichenko, A. E., Decker, M., Fofang, N. T., Liu, S., Gonzales, E., Dominguez, J., Luk, T. S., Neshev, D. N., et al., "Tailoring directional scattering through magnetic and electric resonances in subwavelength silicon nanodisks," ACS Nano **7**(9), 7824–7832 (2013).
[16] Shcherbakov, M. R., Neshev, D. N., Hopkins, B., Shorokhov, A. S., Staude, I., Melik-Gaykazyan, E. V., Decker, M., Ezhov, A. A., Miroshnichenko, A. E., et al., "Enhanced Third-Harmonic Generation in Silicon Nanoparticles Driven by Magnetic Response," Nano Lett. **14**, 6488–6492 (2014).
[17] Carletti, L., Locatelli, A., Stepanenko, O., Leo, G., De Angelis, C., "Enhanced second-harmonic generation from magnetic resonance in AlGaAs nanoantennas," Opt. Express **23**(20), 26544 (2015).
[18] Rose, A., Huang, D., Smith, D. R., "Nonlinear interference and unidirectional wave mixing in metamaterials," Phys. Rev. Lett. **110**(6), 063901 (2013).
[19] Shcherbakov, M. R., Shorokhov, A. S., Neshev, D. N., Hopkins, B., Staude, I., Melik-Gaykazyan, E. V., Ezhov, A. A., Miroshnichenko, A. E., Brener, I., et al., "Nonlinear Interference and Tailorable Third-Harmonic Generation from Dielectric Oligomers," ACS Photonics **2**, 578–582 (2015).
[20] Gehrsitz, S., Reinhart, F. K., Gourgon, C., Herres, N., Vonlanthen, A., Sigg, H., "The refractive index of AlxGa1−xAs below the band gap: Accurate determination and empirical modeling," J. Appl. Phys. **87**(11), 7825–7837 (2000).
[21] Grahn, P., Shevchenko, A., Kaivola, M., "Electromagnetic multipole theory for optical nanomaterials," New J. Phys. **14** (2012).
[22] De Ceglia, D., Vincenti, M. A., De Angelis, C., Locatelli, A., Haus, J. W., Scalora, M., "Role of antenna modes and field enhancement in second harmonic generation from dipole nanoantennas," Opt. Express **23**(2), 1715 (2015).
[23] Celebrano, M., Wu, X., Baselli, M., Großmann, S., Biagioni, P., Locatelli, A., De Angelis, C., Cerullo, G., Osellame, R., et al., "Mode matching in multiresonant plasmonic nanoantennas for enhanced second harmonic generation," Nat. Nanotechnology **10**(5), 412–417, Nature Publishing Group (2015).
[24] Kruk, S. S., Weismann, M., Bykov, A., Mamonov, E., Kolmychek, I., Murzina, T., Panoiu, N., Neshev, D. N., Kivshar, Y. S., "Enhanced Magnetic Second-Harmonic Generation from Resonant Metasurfaces," ACS Photonics **2**, 1007–1012 (2015).
[25] Yang, Z., Chak, P., Bristow, A. D., van Driel, H. M., Iyer, R., Aitchison, J. S., Smirl, A. L., Sipe, J. E., "Enhanced second-harmonic generation in AlGaAs microring resonators," Opt. Lett. **32**(7), 826–828 (2007).
[26] Pu, M., Hu, H., Ottaviano, L., Semenova, E., Vukovic, D., Oxenlowe, L. K., Yvind, K., "AlGaAs-On-Insulator Nanowire with 750 nm FWM Bandwidth, -9 dB CW Conversion Efficiency, and Ultrafast Operation Enabling Record Tbaud Wavelength Conversion," Opt. Fiber Commun. Conf. Post Deadline Pap., Th5A.3, Optical Society of America (2015).
[27] Savanier, M., Ozanam, C., Lanco, L., Lafosse, X., Andronico, A., Favero, I., Ducci, S., Leo, G., "Near-infrared optical parametric oscillator in a III-V semiconductor waveguide," Appl. Phys. Lett. **103**(26), - (2013).
[28] Dallesasse, J. M., Deppe, D. G., "III-V oxidation: Discoveries and applications in vertical-cavity surface-emitting lasers," Proc. IEEE **101**(10), 2234–2242 (2013).

ACKNOWLEDGEMENT

The paper and the participation of all the authors has been made in the framework of the Erasmus Mundus NANOPHI project. L. Carletti, C. De Angelis and A. Locatelli acknowledge financial support from U.S. Army ("Engineering second order nonlinear effects in optical antennas") and CARIPLO ("SHAPES - Second-HArmonic Plasmon-Enhanced Sensing"). G. Leo and Q. Stepanenko acknowledge financial support from the DOLPHIN project of the SEAM (Science and Engineering of Advanced Materials and Devices) Labex of Sorbonne Paris Cité.